Acta Materialia 226 (2022) 117603

Contents lists available at ScienceDirect

Acta Materialia

journal homepage: www.elsevier.com/locate/actamat

Tuning the ceria interfaces inside the dual phase oxygen transport membranes

Ke Ran[a,b,*], Liudmila Fischer[c,d], Stefan Baumann[c], Wilhelm A. Meulenberg[c,d], Kerstin Neuhaus[e], Joachim Mayer[a,b]

[a] Central Facility for Electron Microscopy GFE, RWTH Aachen University, Aachen 52074, Germany
[b] Ernst Ruska-Centre for Microscopy and Spectroscopy with Electrons ER-C, Forschungszentrum Jülich GmbH, Jülich 52428, Germany
[c] Institute of Energy and Climate Research IEK-1, Forschungszentrum Jülich GmbH, Jülich 52428, Germany
[d] Faculty of Science and Technology, Inorganic Membranes, University of Twente, Enschede, AE 7500, The Netherlands
[e] Forschungszentrum Jülich GmbH, Institute of Energy and Climate Research IEK-12, Helmholtz-Institute Münster, Münster 48149, Germany

ARTICLE INFO

Article history:
Received 26 July 2021
Revised 19 December 2021
Accepted 28 December 2021
Available online 29 December 2021

Keywords:
Dual phase oxygen transport membranes
solute and non-solute grain boundary segregation
aberration-corrected STEM HAADF
EELS
EDXS

ABSTRACT

Dual-phase oxygen transport membranes (DP-OTMs) offer a good alternative for the separation of oxygen from gas mixtures. As a promising candidate, the overall performance of the fluorite-spinel composite $Ce_xGd_{1-x}O_{2-\delta}$-$Fe_yCo_{3-y}O_4$ (CGO-FCO) is often dominated by the behavior of the CGO-CGO grain boundaries (GBs), such as solute and non-solute segregations and structural disorders within the boundary. Due to the largely unknown atomistic GB environment, any attempt to control the GBs for an optimized membrane performance is still severely limited. In order to bridge this essential gap, utilizing advanced transmission electron microscopy (TEM) techniques, we quantified both atomistic and chemical structures at the CGO GBs inside the CGO-FCO DP-OTMs down to sub-nm scale. The atomic-site specific lattice distortions, elemental distributions, and valence state variations were found to be well confined within ~2 nm around the GB, where a clear dependence on the structural coherence of individual GBs can be established. Our results further unraveled the complicated CGO GB environment inside real DP-OTMs, and paved the path towards optimized processing of various types of functional membranes.

1. Introduction

Along with an outstanding permeation performance, critical requirements for chemical, electrical, thermal and mechanical stabilities must be fulfilled as well, in order to achieve a successful oxygen transport membrane (OTM). Most of the well-established single-phase OTMs (SP-OTMs) belong to the perovskite-type, such as $Ba_{0.5}Sr_{0.5}Co_{0.8}Fe_{0.2}O_{3-\delta}$ (BSCF) and $La_{1-x}Sr_xCo_{1-y}Fe_yO_{3-\delta}$ (LSCF). Major drawback of the SP-OTMs is their limited long-term stability at high temperatures in aggressive atmospheres (CO_2, SO_2 and other reactive gases). [1-3] Dual-phase OTMs (DP-OTMs) on the other hand are composite materials expected to provide efficient oxygen permeation and high stability under practical conditions, in which two ceramic phases are coupled to provide a pure electronic and ionic conducting pathway, respectively. In particularly, a fluorite-spinel composite $Ce_xGd_{1-x}O_{2-\delta}$-$Fe_yCo_{3-y}O_4$ (CGO-FCO) [4] was reported to possess a significant oxygen permeability as well as a high tolerance under exhaust gas conditions, making it a promising candidate for post-combustion carbon capture and sequestration. [57]

Although the properties of both CGO and FCO can be well tuned separately, [8, 9] the overall performance of the DP-OTMs is also determined by the phase interaction and the nature of the interfaces such as grain boundaries (GBs). Subtle segregations at the GBs [10, 11] can lead to significantly different atomic bonding environments compared to the grain interior, including coordination deficient sites, dangling bonds, and nonstoichiometric terminations. [12, 13] Owing to their local chemical inhomogeneity and complex structure, the GBs often exhibit unusual mechanical, [12, 14] electrical, [13, 15] and chemical properties [16, 17] which may not exist in the bulk crystals but govern the overall properties of the materials. [12 16, 18 21] In this respect, controlling the GB properties offers the possibility of materials engineering, which requires however a precise understanding of the structure and chemistry of the GBs down to atomic scale.

Enabled by advanced transmission electron microscopy (TEM) techniques, the local structure and chemistry of GBs can be directly revealed by scanning transmission electron microscopy (STEM) combined with energy-dispersive X-ray spectroscopy (EDXS) and

* Corresponding author.
E-mail address: ran@gfe.rwth-aachen.de (K. Ran).

https://doi.org/10.1016/j.actamat.2021.117603
1359-6454/

electron energy loss spectroscopy (EELS). For several ceramics, the atomic-site specific manner of impurity atom segregation has been proven, revealing a clear relationship between local GB non-solute segregation and resultant physical properties. [1214] However, solute segregation is still extremely challenging to identify experimentally at the atomic scale, [22, 23] which critically hinders the control of GBs and the related properties of many technologically important materials.

In this work, we will study the DP-OTMs based on CGO-FCO, in which the bottleneck of the overall performance mainly comes from the fluorite CGO. [24] For single-phase CGO, its GB conductivity was reported to be several orders of magnitudes lower than its bulk conductivity. [19, 25] Thus, our interests are particularly focused on the CGO GBs inside the CGO-FCO. In spite of the experimental challenges to resolve the individual atomic columns across the CGO GBs due to the polycrystalline nature of the composite, we will compare a Σ3 [110] CGO GB with a less coherent one, regarding the disordered atomic structures, solute and non-solute segregations, varying valence states, as well as the behaviors of the oxygen vacancies (V_Os). With quantitative structural analysis and chemical mapping down to sub-nm scale, our results will shed light on the true understanding of the CGO GBs inside real DP-OTMs, and provide valuable insights into the fine tuning of GB properties from various aspects.

2. Materials and methods

Pellets with the nominal compositions $Ce_{0.8}Gd_{0.2}O_{2-\delta}$-$Fe_2CoO_4$ (CGO20-F2CO) and $Ce_{0.9}Gd_{0.1}O_{2-\delta}$-$FeCo_2O_4$ (CGO10-FC2O) were prepared by the solid state reactive sintering (SSRS) method. The nominal phase mixture, i.e. not considering any phase reactions between CGO and FCO, was 60:40 wt%. Respective amounts of commercially available powders of CGO20 (Treibacher Industrie AG, Austria) or CGO10 (grade UHSA, Solvay, Belgium) as well as Fe_2O_3 and Co_3O_4 (Sigma-Aldrich, Germany) were homogenized in ethanol using zirconia milling balls. After drying, the powder mixtures were dry pressed into pellets and sintered at 1200°C for 10 hours. During cooling between 900 and 800°C, a low rate of 0.5 K/min was introduced in order to re-oxidize the high temperature rock salt to the desired spinel phase. [4]

TEM specimens were cut from the CGO-FCO pellets by focused ion beam (FIB) milling using an FEI Strata400 system with Ga ion beam. Further thinning and cleaning were performed with an Ar ion beam in a Fischione Nanomill 1040 at 900 eV and 500 eV beam energy respectively. TEM and energy-filtered TEM (EFTEM) imaging were performed by FEI Tecnai F20 at 200 kV. High resolution high-angle annular dark-field (HAADF) imaging, EDXS chemical mapping and EELS spectrum imaging (EELS SI) with atomic resolution were conducted with an FEI Titan G2 80-200 ChemiSTEM microscope equipped with an XFEG, a probe Cs corrector, a super-X EDXS system, and a Gatan Enfinium ER (model 977) spectrometer with DUAL EELS acquisition capability. [26] The convergence semi-angle for STEM imaging and EDXS chemical mapping was approximately 22 mrad, while the collection semi-angles were 80-220 mrad for HAADF imaging and around 47 mrad for EELS SI. EDXS maps were collected typically for around 10 minutes, and background subtraction was performed. EELS SIs were recorded with 0.5 eV per channel energy dispersion and 0.1 s dwell time for each pixel. Energy drift was corrected by aligning the zero-loss peak (ZLP) that was acquired simultaneously with core edges via dual EELS mode. Multivariate statistical analysis (MSA) was performed to reduce the noise of the ELL spectra with weighted principle-component analysis (PCA). To improve the image quality, the HAADF images were first averaged from a series of frames with a relatively short exposure time by an iterative rigid alignment algorithm, and then smoothed by a non-linear filtering algorithm. [27] Structural models were visualized with VESTA. [28]

3. Results

The representative grain and phase distribution inside the DP-OTMs are shown in Fig. 1a, based on a nominal $Ce_{0.9}Gd_{0.1}O_{2-\delta}$-$FeCo_2O_4$ with 60:40 wt.% ratio (60CGO10-FC2O). A grain size of ~ hundreds of nms can be determined for both phases from the top TEM image. The corresponding EFTEM image at the bottom in Fig. 1a separates the two phases, CGO10 in red and FC2O in green, revealing a homogeneous mixture between the two phases. Taking a closer look, Fig. 1b shows the EDXS chemical mapping results from a junction of three CGO10 grains, G1, G2 and G3. Among them, G1 is oriented along the [101] direction and thus appears brighter than G2 and G3, which are both randomly oriented. Within the bulk regions, all the elemental maps show uniform intensities, indicating a homogenous Gd substitution of Ce and no significant agglomeration of V_Os. Along the GBs, the dark linear contrast labeled as A, B and C in the HAADF image in Fig. 1b, a significant loss of Ce as well as evident enrichments of Gd, Fe and Co can be detected simultaneously. In the O map, relatively lower intensities along the GBs can also be noticed. Taking GB A as an example, along the arrow across it, the intensity variations of different elements are plotted in Fig. 1c. Furthermore, the observed enrichment/depletion of each element shows a certain dependence on the GBs. Qualitatively, the GB intensities in the Gd, Fe and Co maps are in an order of A > B > C.

These experimentally observed GB-dependent chemical variations are a joint result of the effective elemental distributions, the relative orientations and the contacting planes between adjacent grains, any thickness or density alterations across the GB, as well as the viewing direction. Thus, by probing the true structural and chemical disorders at the GBs, all these factors need to be taken into consideration.

3.1. The Σ3 [101] CGO20 grain boundary, structural analysis

At the atomic scale, in order to precisely correlate the structural and chemical behaviors around the GB, any geometric factors which might shadow the actual elemental distribution or compromise the imaging quality should be avoided. The HAADF image in Fig. 2a shows a Σ3 [101] GB found inside a 60CGO20-F2CO composite, where Σ denotes the degree of geometrical coincidence of the crystalline interface. The two grains in Fig. 2a, G1 and G2, are oriented along [101], and contacting with the (1-1-1) planes. Relatively darker contrast at the GB (Layer 0) can be observed. On the right side of Fig. 2a, a profile of the spacing between neighboring (1-1-1) planes is plotted. Around Layer 0, 2.78±0.02 Å and 2.68±0.02 Å are determined, while an averaged value of 3.19±0.02 Å is estimated from the remaining layers. Since both Fe and Co are taking the Ce sites along the GB (as will be discussed later), these reduced layer spacings can be reasonably explained by the relatively smaller atomic radii of Fe and Co than Ce and/or Gd. [29]

The rotated rectangle in Fig. 2a defines the region for further EDXS chemical mapping, and the corresponding elemental maps of Ce *L*, Gd *L*, Fe *K*, Co *K* and O *K* lines, together with a composite map of Ce and Fe are shown in Fig. 2b. Around the GB, both G1 and G2 end up with simultaneous Ce depletion and Gd enrichment within single (1-1-1) planes. The segregated of Fe and Co stay in between the two grains, also limited to a single (1-1-1) plane. Besides, a slight drop of intensity in the O map can be noticed around the interface.

In addition to the chemical distribution, structural analysis was also applied to Fig. 2a. Fig. 2c,d map the lattice variations, δ_{xx} and δ_{yy}, taking the dashed-rectangle-defined regions as references. The

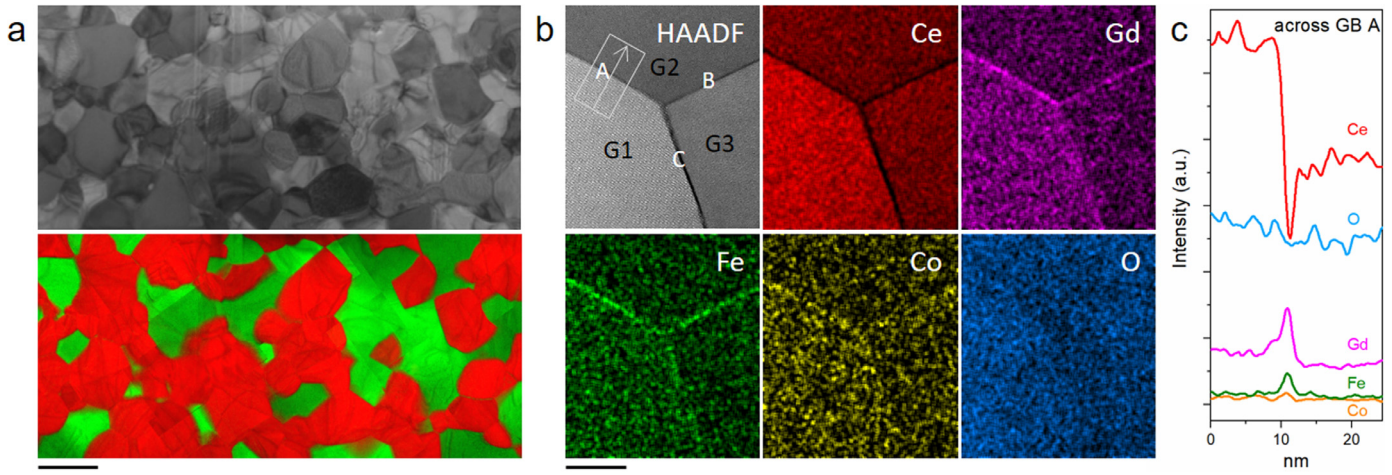

Fig. 1. Overview of a CGO10-FC2O DP-OTM with a 60:40 wt.% ratio. (a) TEM image and the corresponding EFTEM image showing the grain size and phase distribution inside the DP-OTM (red: Ce and thus representing CGO10, green: Co and thus representing FC2O). Scale bar is 1 μm. (b) The EDXS chemical mapping results from a junction of three CGO10 grains (G1, G2 and G3 with the grain boundaries A, B and C): HAADF image and the elemental maps in intensity from the Ce *L* line, Gd *L* line, Fe *K* line, Co *K* line and O *K* line. Scale bar is 20 nm. (c) The EDXS intensities of different elements along the arrow across grain boundary A, as defined in the HAADF image in (b).

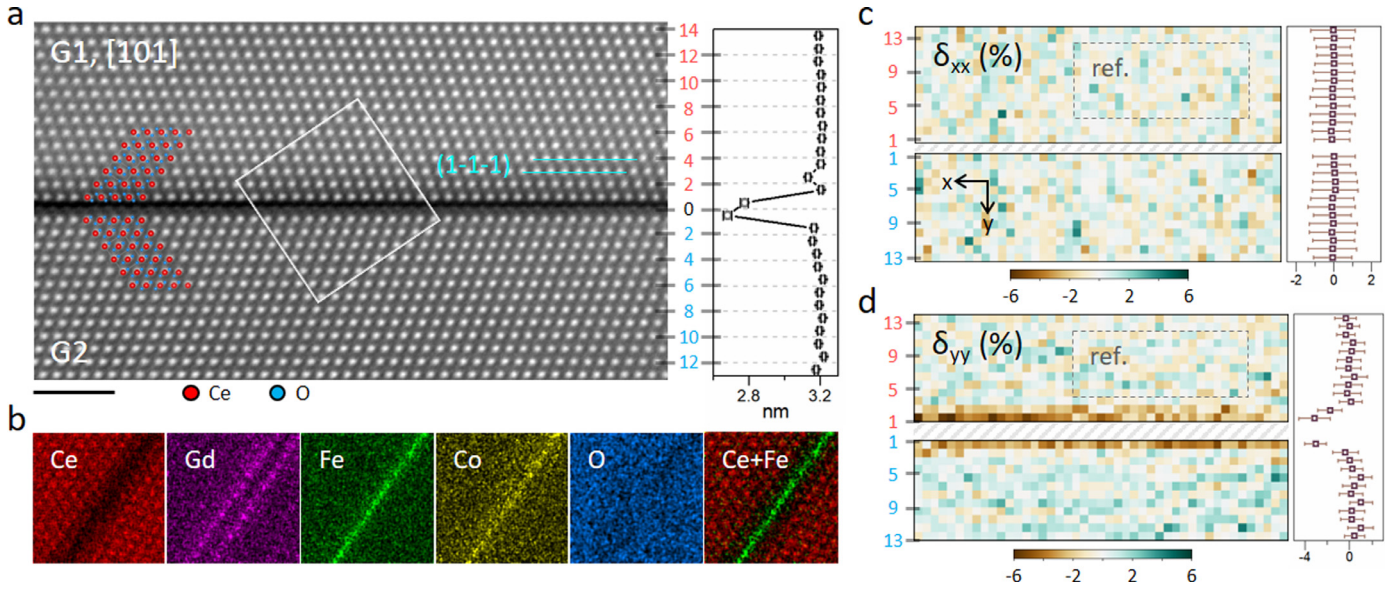

Fig. 2. The Σ3 [101] CGO20 GB. (a) HAADF image around the GB. The two grains, G1 and G2, are oriented along the [101] direction, and contacting with the (1-1-1) planes. Structural models of CeO_2 oriented correspondingly are overlaid on the image. The rotated rectangle defines the region for further EDXS chemical mapping. On the right side of (a) plots the spacings between neighboring (1-1-1) planes. Scale bar is 2 nm. (b) EDXS elemental maps in intensity from the Ce *L*, Gd *L*, Fe *K*, Co *K* and O *K* lines, together with a composite map of Ce and Fe, corresponding to the rotated rectangle in (a). (c-d) Maps of the lattice variations, δ_{xx} and δ_{yy} in percentage, from G1 and G2. On the right are the laterally averaged variations for each atomic plane with the standard deviations.

Layer 0 is however not considered due to the low accuracy in locating individual atomic columns within the GB. On the right side of Fig. 2c,d are the laterally averaged δ_{xx} and δ_{yy} with their standard deviations. Based on the δ_{xx} map, mainly random oscillations close to zero can be determined. For the δ_{yy}, lattice variations up to -6% is located around the GB.

3.2. EELS analysis of the Σ3 [101] CGO20 grain boundary

The EDXS mapping in Fig. 2b offers a qualitative interpretation of the chemical disorders in the GB vicinity. On the other hand, the GB conductivity is also highly sensitive to the valence state of Ce or any other segregated elements there, as well as the behaviors of V_Os. Therefore, EELS with the ability to probe the electronic properties of different elements as a complementary technique is further employed.

Around the Σ3 [101] GB as in Fig. 2, Fig. 3a is the simultaneously recorded annular dark-field (ADF) image from an EELS SI. On the right side of Fig. 3a, each (1-1-1) plane is labeled from 1 to 10. The extracted elemental maps in intensity from the EELS SI are displayed in Fig. 3b, including the Ce $M_{4,5}$, Gd $M_{4,5}$, O *K*, Fe $L_{2,3}$, Co $L_{2,3}$ edges, and a composite map of Ce and Fe. In general, Fig. 3b is in a good agreement with the EDXS results in Fig. 2b. In Fig. 3f, the laterally averaged intensity profiles from Fig. 3a-b are plotted. Accompanied with the ADF intensity drop around the GB, the Ce depletion starts from Layer 4 and 8, and reaches its minimum at Layer 6. The Gd is mostly enriched at Layer 5 and 7, but depleted again at Layer 6. The O map in Fig. 3b fits well with the CeO_2 crystal model, showing however in Fig. 3f an obviously broadened and higher peak at Layer 6 instead of an expected local minimum. Meanwhile, both the Fe and Co intensity profile share similar features, i.e. segregated primarily to Layer 6 and extended slightly to

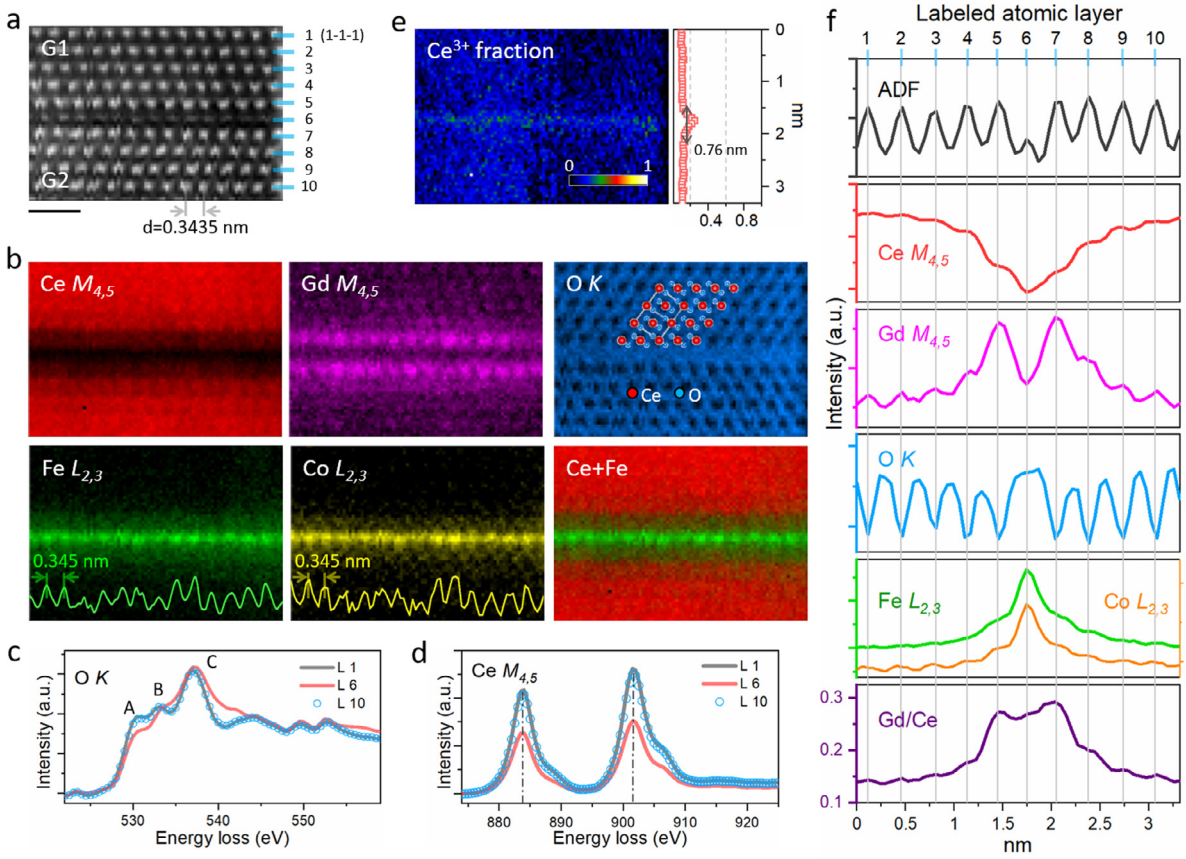

Fig. 3. STEM-EELS analysis of the Σ3 [101] GB. (a-b) The simultaneously recorded ADF image, extracted elemental maps in intensity from Ce $M_{4,5}$, Gd $M_{4,5}$, O *K*, Fe $L_{2,3}$ and Co $L_{2,3}$ edges, together with a composite map of Ce and Fe from the EELS SI. At the bottom of the Fe and Co maps in (b) are the lateral intensity profiles along Layer 6. Scale bar is 1 nm. (c)/(d) Fine structures of the O *K* /Ce $M_{4,5}$ edge corresponding to Layer 1, 6 and 10, as labeled in (a). (e) The Ce^{3+} fraction estimated over the whole mapping area, and its averaged profile across the GB. (f) The laterally averaged intensity profiles from the ADF image and each element (Ce, Gd, O, Fe and Co), and the Gd/Ce ratio across the GB. At the top, the atomic planes are labeled following (a).

Layer 5 and 7. Moreover, at the bottom of the Fe and Co maps in Fig. 3b, the intensity profiles along Layer 6 are extracted. A periodic spacing of ~0.345 nm can be determined, which fits well with the determined distance d=0.3435 nm as indicated at the bottom of the ADF image in Fig. 3a. Besides, the Gd/Ce ratio across the GB is plotted at the bottom of Fig. 3f. Taking the value at Layer 1 as a reference, the Gd/Ce ratios at Layer 5-7 are about doubled (from ~0.14 to ~0.28).

Fig. 3c compares the fine structures of O *K* edges among Layer 1, 6 and 10, after background subtraction. Three peaks, A, B and C, are denoted. Comparing with Layer 1 and 10 which are both far away from the GB, Layer 6 leads to a comparable curve in Fig. 3c, but with an evidently lower Peak A and a much broader peak C. In addition to O, the fine structures of Ce $M_{4,5}$ edges from Layer 1, 6 and 10 are compared in Fig. 3d as well. Except the relatively lower intensity from Layer 6, the fine structure of Ce $M_{4,5}$ edges from all three layers are quite similar, without any significant shift as indicated by the dotted lines. Due to the change of local oxygen chemical potential during thermal treatment and competition for oxygen between adjacent grains, [3032] mixed Ce^{3+} and Ce^{4+} are generally expected to occupy the Ce sites at the CGO interfaces. [33] Previous study showed that the Ce-M_5/Ce-M_4 intensity ratio (R) in second derivative spectra is sensitive to the valence state of the Ce ions. [34] Using pure standards, R was determined as 0.925 and 1.25 for Ce^{4+} and Ce^{3+} respectively, and the Ce^{3+} fraction (x) can be approximately estimated by R=0.925(1-x)+1.25x. [35] Following this method, Fig. 3e then maps the estimated x, and plots its averaged variation across the GB. Inside both grains, x is around 0, corresponding to an almost pure Ce^{4+} occupation at each Ce site. Around the GB, a narrow peak shows up with a height of ~0.25, suggesting a partial occupation of Ce^{3+} at the Ce sites.

3.3. The asymmetric CGO10 grain boundary, viewed edge-on

In contrast to the Σ3 [101] CGO20 GB as in Fig. 2,3, the HAADF image in Fig. 4a shows an asymmetric one found inside a 60CGO10-FC2O composite, by tilting the sample until both CGO10 grains were viewed edge-on. The upper and lower grains, G1 and G2, are oriented along the [101] and [114] directions respectively, and contacting with the (1-1-1) and (1-51) planes. All the (1-1-1) planes from G1 are labeled on the right side of Fig. 4a, from 1 to 12. A much lower contrast ~0.4 nm thick along the GB can be noticed.

For the same GB, Fig. 4b shows the EDXS chemical mapping results, where the dashed line roughly separates G1 and G2. The most evident chemical disorders are mainly confined within one or two atomic layers on both sides of the GB. For G1, significant loss of Ce can be noticed along the last two (1-1-1) planes. In contrast, Gd shows an above average occupation of the Ce sites in the second last (1-1-1) plane, but almost disappears in the last plane. The enrichment of Fe can be located along the last (1-1-1) plane, while any solid conclusion about the Co is hard to draw due to the low intensity from the Co map in Fig. 4b. In addition, inside the O map, the intensity drops slightly around the GB as well. For G2, subject to the narrow spacing between (1-51) planes, of ~1 Å, resolving individual atoms is experimentally challenging. However,

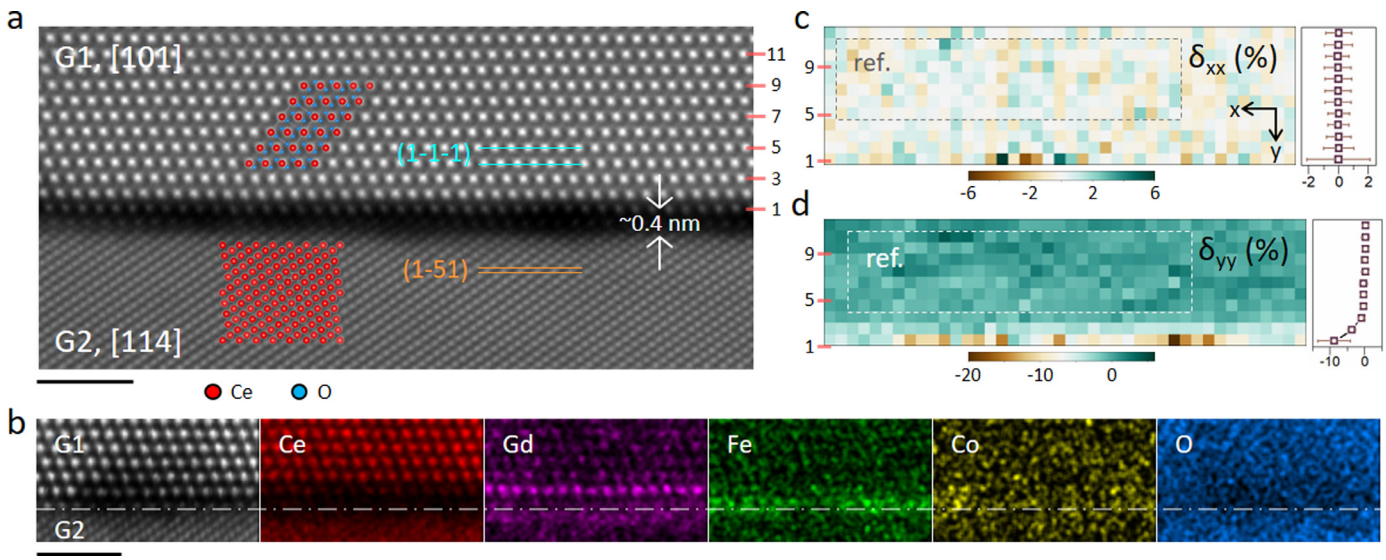

Fig. 4. The asymmetric CGO10 GB. (a) HAADF image around the GB between G1 and G2. The two grains are oriented along the [101] and [114] directions, and contacting with their (1-1-1) and (1-51) planes. Structural models of CeO_2 oriented correspondingly are overlaid on the image. (b) EDXS chemical mapping around the same GB: HAADF image, and the elemental maps in intensity from Ce *L*, Gd *L*, Fe *K*, Co *K* and O *K* lines. The dashed line roughly separates G1 and G2. (c-d) Maps of the lattice variations, δ_{xx} and δ_{yy} in percentage, from G1, with the atomic planes labeled on the left. On the right are the laterally averaged variations for each atomic plane with the standard deviations. Scale bars are 2 nm.

the elemental mapping is still able to reveal similar chemical disorders in the vicinity of the GB as in G1, i.e. the loss of Ce and O accompanied with the enrichment of Gd and Fe.

Similar as in Fig. 2, structural analysis was applied to Fig. 4a. Fig. 4c,d map the lattice variations, δ_{xx} and δ_{yy} in percentage, covering the labeled planes by taking the dashed-rectangle-defined regions as references. In Fig. 4c, the estimated δ_{xx} is jumping slightly around zero, except a few random oscillations within Layer 1, leading to a relatively higher deviation. In contrast, in Fig. 4d, distinct variations up to -30% are determined at both Layer 1 and 2, leading to an abrupt drop of the averaged δ_{yy} from 0 to ~ -10%. Thus, at this asymmetric GB, the parallel contacting planes (1-1-1) and (1-51) from G1 and G2 result in ignorable structural disorders in the lateral direction. Vertically, partially due to the significantly different plane spacing, $d_{(1\text{-}1\text{-}1)} \approx 3.13$ Å and $d_{(1\text{-}51)} \approx 1.04$ Å, substantial lattice variations are measured in G1, but only limited to the first few atomic planes.

3.4. EELS analysis of the asymmetric CGO10 grain boundary

Following the same procedure as in Fig. 3, Fig. 5 shows the corresponding EELS analysis on the asymmetric GB. On the right side of Fig. 5a, each (1-1-1) plane from G1 is labeled from 1 to 6, and the first two (1-51) planes from G2 are labeled as b1 and b2. The elemental maps in intensity are displayed in Fig. 5b, and Fig. 5f plots the laterally averaged intensity profiles from Fig. 5a,b. Obviously, all the ADF, Ce and O signals drop around the GB, while the Gd enriches significantly at the second last layers (Layer 5 and b2) but accompanied with clear drops at the last layers (Layer 6 and b1). In addition, the segregations of Fe and Co are mainly located around Layer 6 and b1, but also at Layer 5 and b2 with reduced intensities. The Gd/Ce ratio across the GB is plotted at the bottom of Fig. 5f. Taking the value at Layer 1 as a reference, at Layer 5 and Layer 6, the Gd/Ce ratio are almost quadrupled (from ~0.14 to ~0.51).

As defined by the brackets on the right in Fig. 5b, three different regions are labeled as R1, R2 and R3. Fig. 5c and 5d compare the fine structures of O *K* and Ce $M_{4,5}$ edges among these regions. In Fig. 5c, the curve from R2 is much weaker and flatter, while those from R1 and R3 are showing similar fine structures with comparable intensities. Meanwhile, in Fig. 5d, the Ce $M_{4,5}$ edge from R2 is much lower, accompanied with clear shifts of both M_5 and M_4 edges as indicated by the dotted lines. These shifts are also reflected in Fig. 5e, where the Ce^{3+} fraction raises rapidly to 1 and indicates a pure Ce^{3+} occupation of the Ce sites at the GB core.

4. Discussion

The present study is related to two composites, CGO20-F2CO and CGO10-FC2O, both with a 60:40 wt.% ratio. The reported CGO GB features here, i.e. the simultaneous Ce depletion and Gd enrichment at the last atomic layers of CGO grains, and the segregated Fe and Co between neighboring CGO grains, are consistently observed in both cases, irrespective of the nominal Gd/Ce or the Fe/Co ratios in the composites. Furthermore, the Gd/Ce ratios determined from the grain interiors are ~0.14 in both Fig. 3f and 5f, indicating a similar effective Gd substitution of Ce inside CGO10 and CGO20. Any excessive Gd will then play an important role in the phase interaction between the fluorite and spinel phase (Supplementary information, Fig. S1), and any reduction at the other types of interfaces inside the DP-OTM is rather ignorable, which are beyond the scope of this study.

Comparing Fig. 3 and 5, the different behaviors of Ce^{3+} fraction and Gd/Ce ratio between the two GBs are obvious (Supplementary information, Table S1). It has been reported that nonstoichiometric terminations and/or the breaking cation-anion bonding distributions at the GBs could cause a local spatial charge inhomogeneity and attract the negatively charged $Ce^{3+}{}_{Ce}$ and Gd_{Ce}. [3638] For the Σ3 [101] GB, as shown in Fig. 2c,d, only local and trivial lattice variations are detected perpendicular to the GB plane. The segregated mainly Fe and a few Co are confined within single (1-1-1) planes, which are showing a consistent lattice parameter as the bulk CGO. Thus, at the core of this atomically coherent GB configuration, only limited imbalanced charges are expected. As a result, in Fig. 3e, around the GB core, the Ce^{3+} fraction only raises slightly from 0 to ~0.25 within a limited range ~0.76 nm, while the Gd/Ce ratio is about doubled in Fig. 3f. In contrast, for the asymmetric GB, Fig. 4d indicates considerable δ_{yy} up to -30% perpendicular to the GB. No certain patterns can be determined for the segregated Fe or

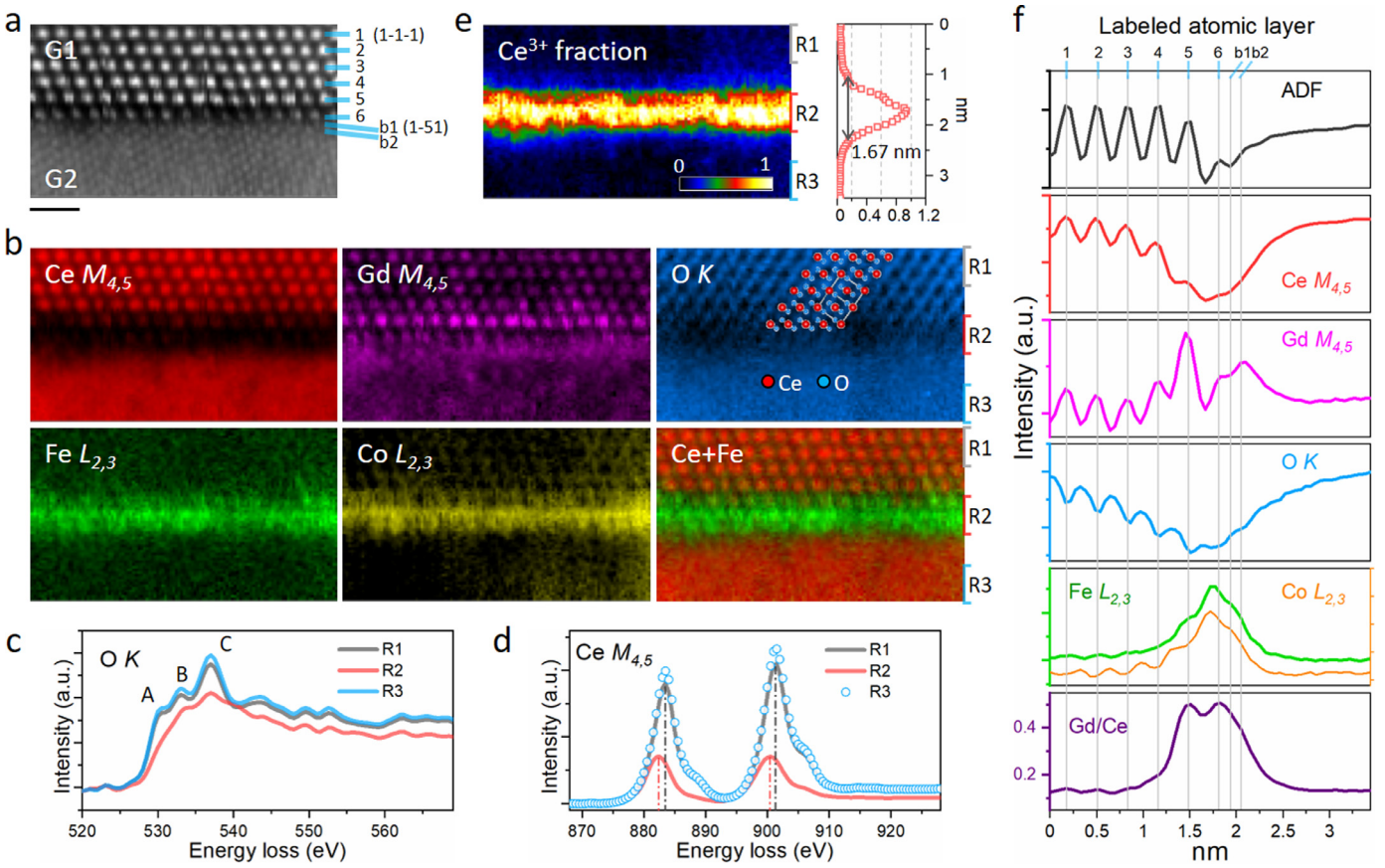

Fig. 5. STEM-EELS analysis of the asymmetric GB as shown in Fig. 4. (a-b) The simultaneously recorded ADF image, extracted elemental maps in intensity from Ce $M_{4,5}$, Gd $M_{4,5}$, O *K*, Fe $L_{2,3}$ and Co $L_{2,3}$ edges, together with a composite map of Ce and Fe from the EELS SI. Scale bar is 1 nm. (c)/(d) Fine structures of the O *K*/Ce $M_{4,5}$ edge integrated from the regions R1, R2 and R3 as defined by the brackets on the right side of (b). (e) The Ce^{3+} fraction estimated over the whole mapping area, and its averaged profile across the GB. (f) The laterally averaged intensity profiles from the ADF image and each element (Ce, Gd, O, Fe and Co), and the Gd/Ce ratio across the GB. At the top, the atomic planes are labeled following (a).

Co. Thus, more imbalanced charges would be produced at this incommensurate GB structure. Consequently, around the GB core in Fig. 5e, the Ce^{3+} fraction ratio increases significantly from 0 to 1 within a broader range of ~1.67 nm. Meanwhile, the ratio of Gd/Ce is almost quadrupled in Fig. 5f. Thus, the enrichment of $Ce^{3+}{}_{Ce}$ and Gd_{Ce} are effectively mitigated in the vicinity of GBs with a higher coherence.

For ionic crystals, the behaviors of V_Os across the GBs are often debatable. As proposed by the classic space charging (SC) theory, [19] intrinsic immobile V_Os are enriched at the GB core, while the mobile V_Os will be depleted in the area adjacent to the GB cores. In contrast, an increased O concentration and thus a depleted V_Os was reported at the GB core of yttria-stabilized zirconia (YSZ), [22] in spite of the directly observed decreased O intensity. Consistent with the YSZ case, the estimated O concentrations from the two GBs in Fig. 6 reach the maxima at the GB cores, while opposite trend between intensity and concentration is noticed in Fig. 6b (Supplementary information, Fig. S2). However, both electron channeling and non-solute segregation could complicate the determination of the O concentration. While the channeling effect only plays a minor role here (Supplementary information, Fig. S2), the more critical matter in quantification comes from the segregated Fe and Co with limited compositional and structural information. Around the GB, the detected O intensity is shared between the CGO and the segregated Fe and Co, yet the amount and phase of these non-solute segregations may vary from GB to GB (Supplementary information, Fig. S3). Furthermore, an averaged Fe^{3+} fraction of ~96% can be determined for the segregated Fe, [39] which could also contribute to the fine structures of the O K edge around the GBs, Layer 6 in Fig. 3c and R2 in Fig. 5c. The same estimation for the valence states of Co is however not feasible due to its low intensity (Supplementary information, Fig. S4). Therefore, in order to extract a precise description of the V_Os behaviors, a detailed numerical calculation for individual GBs would be necessary.

Theoretically, the percolation threshold for a DP-OTM is only considered to be reached, if the volume fraction of the minor phase is no less than 30 vol%. [40] Yet, an experimental best performance was found with a volume fraction of only 18.5 vol%, while increased permeation at high temperature can still be detected with even 10 vol%. [4] One way to account for this threshold contradiction would be the alternative electronic conducting paths provided by the segregated Fe and Co at the CGO interfaces. As a result of the phase interaction and depending on the specific composition of the CGO-FCO, the segregated Fe and Co can stay between CGO grains and/or form a tertiary phase (Supplementary information, Fig. S1). [33] Thus, cautiously varying the CGO-FCO composition and the processing procedure might realize a controllable segregation of the Fe and Co at the CGO GBs, and subsequently the building of extra electronic conducting paths in addition to the original FCO phase. Hopefully, the 30% threshold for the minor phase to achieve percolation could be relaxed, and the ionic conduction of the CGO phase could be further improved through an increased CGO component in the DP-OTMs.

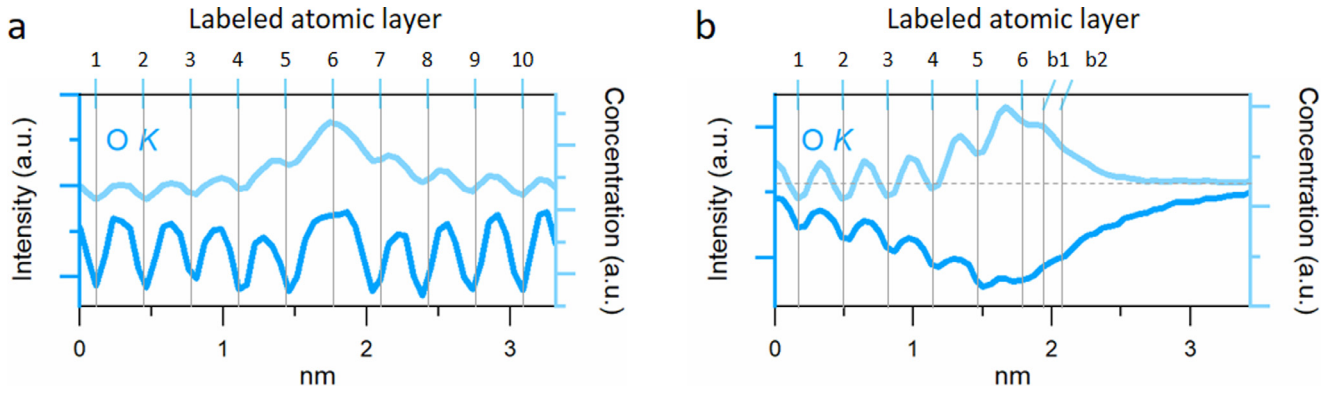

Fig. 6. Comparison between the O intensity and O concentration profiles across the Σ3 [101] CGO20 (a) and the asymmetric CGO10 (b) GB.

5. Conclusion

In summary, the chemical and crystal structures across the CGO GBs inside real DP-OTMs were determined down to the sub-nm scale. Simultaneous Ce enrichment and Gd depletion within the ending atomic layers of the adjacent CGO grains are generally observed, while Fe and Co are segregated into the CGO GBs with varying amounts and phases. The comparison between GBs with different coherencies indicates that the valence states of Ce, and the enriched Gd, Fe and Co are all sensitive to the local structural defects at the GB. A more coherent GB would thus be beneficial for an improved GB conductivity. Moreover, the non-solute segregation of Fe and Co at the CGO GBs could potentially provide alternative electronic conducting paths. Our findings will be a crucial piece for the complete picture of structure-property relationship at GBs, which is indispensable for optimizing the membrane performance through GB engineering and composition manipulation. These results here may also shed light on the understanding towards other oxide heterointerface phenomena, which has been conventionally explained by the SC theory without direct experimental evidences.

Declaration of Competing Interest

The authors declare that they have no known competing financial interests or personal relationships that could have appeared to influence the work reported in this paper.

Acknowledgement

This work has been supported by the Deutsche Forschungsgemeinschaft (Project number 387282673).

Supplementary materials

Supplementary material associated with this article can be found, in the online version, at doi:10.1016/j.actamat.2021.117603.

References

[1] J. Sunarso, S. Baumann, J.M. Serra, W.A. Meulenberg, S. Liu, Y.S. Lin, J.C.D. da Costa, Mixed ionic-electronic conducting (MIEC) ceramic-based membranes for oxygen separation, J. Membrane Sci. 320 (2008) 13–41.
[2] J.M. Serra, J. Garcia-Fayos, S. Baumann, F. Schulze-Kuppers, W.A. Meulenberg, Oxygen permeation through tape-cast asymmetric all-$La_{0.6}Sr_{0.4}Co_{0.2}Fe_{0.8}O_{3-d}$ membranes, J. Membrane Sci. 447 (2013) 297–305.
[3] S. Baumann, J.M. Serra, M.P. Lobera, S. Escolastico, F. Schulze-Kuppers, W.A. Meulenberg, Ultrahigh oxygen permeation flux through supported $Ba_{0.5}Sr_{0.5}Co_{0.8}Fe_{0.2}O_{3-d}$ membranes, J. Membrane Sci. 377 (2011) 198–205.
[4] M. Ramasamy, E.S. Persoon, S. Baumann, M. Schroeder, F. Schulze-Kuppers, D. Gortz, R. Bhave, M. Bram, W.A. Meulenberg, Structural and chemical stability of high performance $Ce_{0.8}Gd_{0.2}O_{2-d}$ - $FeCo_2O_4$ dual phase oxygen transport membranes, J. Membrane Sci. 544 (2017) 278–286.
[5] H.X. Luo, K. Efimov, H.Q. Jiang, A. Feldhoff, H.H. Wang, J. Caro, CO_2-stable and cobalt-free dual-phase membrane for oxygen separation, Angew Chem. Int. Edit. 50 (2011) 759–763.
[6] M. Balaguer, J. Garcia-Fayos, C. Solis, J.M. Serra, Fast oxygen separation through SO_2- and CO_2-stable dual-phase membrane based on $NiFe_2O_4$-$Ce_{0.8}Tb_{0.2}O_{2-d}$, Chem. Mater. 25 (2013) 4986–4993.
[7] H.X. Luo, H.Q. Jiang, T. Klande, Z.W. Cao, F.Y. Liang, H.H. Wang, J. Caro, Novel cobalt-free, noble metal-free oxygen-permeable $40Pr_{0.6}Sr_{0.4}FeO_{3-d}$-$60Ce_{0.9}Pr_{0.1}O_{2-d}$, dual-phase membrane, Chem. Mater. 24 (2012) 2148–2154.
[8] E.J. Verwey, P.W. Haayman, F.C. Romeijn, Physical properties and cation arrangement of oxides with spinel structures .2. electronic conductivity, J. Chem. Phys. 15 (1947) 181–187.
[9] V.V. Kharton, A.V. Kovalevsky, A.P. Viskup, A.L. Shaula, F.M. Figueiredo, E.N. Naumovich, F.M.B. Marques, Oxygen transport in $Ce_{0.8}Gd_{0.2}O_{2-d}$-based composite membranes, Solid State Ionics 160 (2003) 247–258.
[10] R. Gerhardt, A.S. Nowick, Grain-boundary effect in ceria doped with trivalent cations: I, Electrical Measurements J. Am. Ceram. Soc. 69 (1986) 641–646.
[11] H.J. Avila-Paredes, S. Kim, The Effect of segregated transition metal ions on the grain boundary resistivity of gadolinium doped ceria: alteration of the space charge potential, Solid State Ionics 177 (2006) 3075–3080.
[12] J.P. Buban, K. Matsunaga, J. Chen, N. Shibata, W.Y. Ching, T. Yamamoto, Y. Ikuhara, Grain boundary strengthening in alumina by rare earth impurities, Science 311 (2006) 212–215.
[13] Y. Sato, J.P. Buban, T. Mizoguchi, N. Shibata, M. Yodogawa, T. Yamamoto, Y. Ikuhara, Role of Pr segregation in acceptor-state formation at ZnO grain boundaries, Phys. Rev. Lett. 97 (2006) 106802.
[14] J.F. Nie, Y.M. Zhu, J.Z. Liu, X.Y. Fang, Periodic segregation of solute atoms in fully coherent twin boundaries, Science 340 (2013) 957–960.
[15] R.F. Klie, J.P. Buban, M. Varela, A. Franceschetti, C. Jooss, Y. Zhu, N.D. Browning, S.T. Pantelides, S.J. Pennycook, Enhanced current transport at grain boundaries in high-T-c superconductors, Nature 435 (2005) 475–478.
[16] W. Lee, H.J. Jung, M.H. Lee, Y.B. Kim, J.S. Park, R. Sinclair, F.B. Prinz, Oxygen surface exchange at grain boundaries of oxide ion conductors, Adv. Funct. Mater. 22 (2012) 965–971.
[17] B. Feng, I. Sugiyama, H. Hojo, H. Ohta, N. Shibata, Y. Ikuhara, Atomic structures and oxygen dynamics of CeO_2 grain boundaries, Sci. Rep.-Uk 6 (2016) 20288.
[18] N. Shibata, S.J. Pennycook, T.R. Gosnell, G.S. Painter, W.A. Shelton, P.F. Becher, Observation of rare-earth segregation in silicon nitride ceramics at sub-nanometre dimensions, Nature 428 (2004) 730–733.
[19] X. Guo, R. Waser, Electrical properties of the grain boundaries of oxygen ion conductors: acceptor-doped zirconia and ceria, Prog. Mater. Sci. 51 (2006) 151–210.
[20] K. Lu, L. Lu, S. Suresh, Strengthening materials by engineering coherent internal boundaries at the nanoscale, Science 324 (2009) 349–352.
[21] T. Meiners, T. Frolov, R.E. Rudd, G. Dehm, C.H. Liebscher, Observations of grain-boundary phase transformations in an elemental metal, Nature 579 (2020) 375–378.
[22] B. Feng, N.R. Lugg, A. Kumamoto, Y. Ikuhara, N. Shibata, Direct observation of oxygen vacancy distribution across yttria-stabilized zirconia grain boundaries, Acs. Nano. 11 (2017) 11376–11382.
[23] B. Feng, T. Yokoi, A. Kumamoto, M. Yoshiya, Y. Ikuhara, N. Shibata, Atomically ordered solute segregation behaviour in an oxide grain boundary, Nat. Commun. 7 (2016) 11079.
[24] F.L. Zeng, S. Baumann, J. Malzbender, A. Nijmeijer, L. Winnubst, O. Guillon, R. Schwaiger, W.A. Meulenberg, Enhancing oxygen permeation of solid-state reactive sintered $Ce_{0.8}Gd_{0.2}O_{2-\delta}$-$FeCo_2O_4$ composite by optimizing the powder preparation method, J. Membrane Sci. 628 (2021) 119248.
[25] H.J. Avila-Paredes, K. Choi, C.T. Chen, S. Kim, Dopant-concentration dependence of grain-boundary conductivity in ceria: a space-charge analysis, J. Mater. Chem. 19 (2009) 4837–4842.
[26] A. Kovács, R. Schierholz, K. Tillmann, FEI titan G2 80-200 CREWLEY, J. Large-Scale Research Facilities 2 (2016) A43.
[27] K. Ran, W. Deibert, M.E. Ivanova, W.A. Meulenberg, J. Mayer, Direction observa-

tion of the grain boundary segregation in molybdenum substituted lanthanum tungstate membranes, Nanoscale 12 (2020) 17841–17848.
[28] K. Momma, F. Izumi, VESTA 3 for three-dimensional visualization of crystal, volumetric and morphology data, J. Appl. Crystallogr. 44 (2011) 1272–1276.
[29] T.S. Zhang, J. Ma, L.B. Kong, S.H. Chan, P. Hing, J.A. Kilner, Iron oxide as an effective sintering aid and a grain boundary scavenger for ceria-based electrolytes, Solid State Ionics 167 (2004) 203–207.
[30] J. Xue, A. Feldhoff, Ambient air partial internal reduction of NiO in a mixed ionic-electronic conducting ceramic, J. Eur. Ceram Soc. 36 (2016) 3451–3456.
[31] M. Ramasamy, S. Baumann, J. Palisaitis, F. Schulze-Kuppers, M. Balaguer, D. Kim, W.A. Meulenberg, J. Mayer, R. Bhave, O. Guillon, M. Bram, Influence of microstructure and surface activation of dual-phase membrane $Ce_{0.8}Gd_{0.2}O_{2-\delta}$-$FeCo_2O_4$ on oxygen permeation, J. Am. Ceram Soc. 99 (1) (2016) 349–355.
[32] K.P. Song, H. Schmid, V. Srot, E. Gilardi, G. Gregori, K. Du, J. Maier, P.A. van Aken, Cerium reduction at the interface between ceria and yttria-stabilised zirconia and implications for interfacial oxygen non-stoichiometry, Appl. Mater. 2 (2014) 032104.
[33] Y. Lin, S.M. Fang, D. Su, K.S. Brinkman, F.L. Chen, Enhancing grain boundary ionic conductivity in mixed ionic-electronic conductors, Nat. Commun. 6 (2015) 6824.
[34] J.A. Fortner, E.C. Buck, The chemistry of the light rare-earth elements as determined by electron energy loss spectroscopy, Appl. Phys. Lett. 68 (1996) 3817–3819.
[35] P.F. Yan, T. Mori, Y.Y. Wu, Z.M. Li, G.J. Auchterlonie, J. Zou, J. Drennan, Microstructural and chemical characterization of ordered structure in yttrium doped ceria, Microsc. Microanal. 19 (2013) 102–110.
[36] S. Graser, P.J. Hirschfeld, T. Kopp, R. Gutser, B.M. Andersen, J. Mannhart, How grain boundaries limit supercurrents in high-temperature superconductors, Nat. Phys. 6 (2010) 609–614.
[37] N. Shibata, M.F. Chisholm, A. Nakamura, S.J. Pennycook, T. Yamamoto, Y. Ikuhara, Nonstoichiometric dislocation cores in alpha-alumina, Science 316 (2007) 82–85.
[38] E. Tochigi, Y. Kezuka, A. Nakamura, A. Nakamura, N. Shibata, Y. Ikuhara, Direct observation of impurity segregation at dislocation cores in an ionic crystal, Nano Lett. 17 (2017) 2908–2912.
[39] P.A. van Aken, B. Liebscher, Quantification of ferrous/ferric ratios in minerals: new evaluation schemes of Fe L-23 electron energy-loss near-edge spectra, Phys. Chem. Miner. 29 (2002) 188–200.
[40] X.F. Zhu, H.H. Wang, W.S. Yang, Relationship between homogeneity and oxygen permeability of composite membranes, J. Membrane Sci. 309 (2008) 120–127.